Title:

Towards a widely applicable earthquake detection algorithm for fibreoptic and hybrid fibreoptic-seismometer networks

Authors:

T.S. Hudson[1], S. Klaasen[1], O. Fontaine[2], C.A. Bacon[3], K. Jonsdotti[14], A. Fichtner[1]

[1] Department of Earth and Planetary Sciences, ETH Zurich, Switzerland

2 Universite Libre de Bruxelles, Bruxelles, Belgium

[3] Lamont-Doherty Earth Observatory, USA

[4] Icelandic Met Office, Iceland

Submitted to *Geophyiscal Journal International* submitted to *Geophys. J. Int.*

Towards a widely applicable earthquake detection algorithm for fibreoptic and hybrid fibreoptic-seismometer networks

T.S. Hudson[1], S. Klaasen[1], O. Fontaine[2], C.A. Bacon[3], K. Jónsdóttir[4], A. Fichtner[1]

[1] *Department of Earth and Planetary Sciences, ETH Zurich, Switzerland*

[2] *Université Libre de Bruxelles, Bruxelles, Belgium*

[3] *Lamont-Doherty Earth Observatory, USA*

[4] *Icelandic Met Office, Iceland*

Received xxxx.xx.xx

SUMMARY

Distributed Acoustic Sensing (DAS) is a promising technology for providing dense (metre-scale) sampling of the seismic wavefield. However, harnessing this potential for earthquake detection with accurate phase picking and associated localisation remains challenging. Single-channel algorithms are limited by individual channel noise, while machine learning and semblance methods are typically limited to specific geological settings, have no physically-constrained phase association and/or require specific fibre geometries. Here, we present a method that seeks to detect seismicity for any geological setting, applicable for any fibre geometry, and combining both fibreoptic and conventional seismometer data to maximise the information used for detection and source localisation. This method adapts a proven back-migration detection method to also include DAS observations, propagating energy from many receivers back in time to search for localised peaks in energy, corresponding to seismic sources. The strengths of this method are capitalising on coherency over many channels to enhance detection sensitivity even in high-noise environments compared to single-channel algorithms, applicability to arbitrary fibre geometries, as well as built-in, physics-informed phase association and source localisation. We explore the performance of the method using three geologically and geometrically diverse settings: a glacier, a volcanic eruption and a geothermal borehole. Our results evidence the effect of spatial-sampling extent and non-optimal fibreoptic geometries, accounting for P and S wave sensitivity, coupling effects, and how the sensitivity of native fibreoptic strain measurements to shallow subsurface heterogeneities can affect detection. Finally, we attempt to also present a method-ambivalent overview of key challenges facing fibreoptic earthquake detection and possible avenues of future work to address them.

Key words: seismology, distributed acoustic sensing, earthquake detection, network seismology, computational seismology

1 INTRODUCTION

Earthquakes are essential monitoring various natural hazards, imaging subsurface structure and interrogating various Earth system processes. In order to harness the potential of earthquakes for either monitoring or insight into fundamental processes, one first has to detect and locate any seismicity. Typically, earthquake detection has been performed using conventional seismometers sensitive to the seismic velocity wavefield, but recent new optical instrumentation now allows one to use fibreoptic cables to measure the seismic strain wavefield with far denser spatial sampling over a wide bandwidth [Hartog et al., 2018, Lindsey and Martin, 2021, Lindsey et al., 2020a, Paitz et al., 2021]. This technology is often referred to as Distributed Acoustic Sensing (DAS). However, currently these fibreoptic technologies only provide single-component measurements, with deployed fibre geometries often not favourable for earthquake detection and/or location. Therefore, there is a need for earthquake detection algorithms that can: firstly, be applied for arbitrary fibre geometries; secondly, maximise the spatial sampling extent of the seismic wavefield by combining fibreoptic and conventional seismometer data; and thirdly, capitalise on the spatio-temporal coherency of the earthquake wavefield.

Earthquake detection methods can be broadly separated into two categories: (1) receiver-by-receiver detection, with earthquake arrivals triggered on each seismogram in isolation and then combined afterwards using some form of phase association; or (2) multi-receiver detection, where earthquake arrivals at multiple receivers are combined together in a physics-constrained framework. Common receiver-by-receiver algorithms are applied in the time-domain using short-term-average to long-term-average (STA/LTA) methods, for example [Allen, 1978, Withers et al., 1998], or in the frequency-domain by looking for energy peaks within a certain frequency band [Helmstetter et al., 2015, O'Neel et al., 2007]. Machine-learning techniques, such as convolutional neural networks, have also been applied to receiver-by-receiver seismic phase detection [Mousavi et al., 2020, Zhu and Beroza, 2019, Zhu et al., 2023, Hernandez et al., 2022]. Recently, novel hybrid algorithms combining multiple STA/LTA functions with machine-learning have also been developed [Latto et al., 2024]. Perpetual limitations of any receiver-by-receiver method are not using spatio-temporal coherency information and the challenge of associating phase arrivals from each receiver with one another, especially for multiple wave types [Ross et al., 2019a]. Multi-receiver detection methods overcome these limitations by identifying coherent signals arriving at multiple receivers. Methods that do not explicitly require knowledge of the medium′s velocity structure, designed specifically for DAS measurements include: semblance-based coherence [Porras et al., 2024]; and machine-learning based image recognition methods [Stork et al., 2020, Huot et al., 2022]. More general approaches include array-processing techniques, such as beamforming [Hudson et al., 2023] or covariance matrix analysis [Seydoux et al., 2016]. However, although these methods do not explicitly require subsurface velocity structure information, they either implicitly assume, learn or are sensitive to the local velocity structure. A final multi-receiver method of note is back-migration, which explicitly requires an estimate of velocity structure in the region of interest, using this information to effectively perform physics-informed stacking of energy arriving at multiple receivers [Drew et al., 2013, Hudson et al., 2019, Smith et al., 2020, Winder et al., 2021, Hudson et al., 2021, Guidarelli et al., 2020, Wagner et al., 2017].

When discussing earthquake detection, we deem it helpful to consider the following key ingredients for optimal earthquake detection algorithm performance:

(i) Maximise spatial coverage and sampling density

(ii) Exploit signal coherency

(iii) Maximise sensitivity to multiple seismic phases

(iv) Quantify event origin-time and phase arrival-time uncertainty

(v) Optimise computational efficiency

(vi) *(Bonus: Towards universal applicability, while considering the trade-off with computational efficiency)*

In this work we quantify how important these ingredients are for earthquake detection and evidence the reasons why, relating them to the modifications required to apply an existing back-migration earthquake detection method to fibreoptic and hybrid fibreoptic-seismometer datasets. This builds on previous work, where back-migration was applied to a DAS dataset without any DAS-specific adaptations [Hudson et al., 2021]. While we focus here on local to regional micro-seismicity applications, these ingredients should generally be transferable to global earthquake detection [Selby, 2011] and noise localisation applications [Igel et al., 2023]. We favour a back-migration method because it includes all the key ingredients specified above in the recipe. In particular, the adapted back-migration method presented here allows one to use arbitrary fibreoptic deployment geometries, maximise spatial coverage and seismic phase sensitivity by also including conventional seismometer data, and requires no further modification or retraining when applied to new datasets. It also provides earthquake location estimates without additional cost. Using fibre-optic (DAS) datasets for earthquake detection requires various specific considerations, including: in-axis fibre directional sensitivity, the use of native strain/strain-rate measurements, coupling of the fibre to the medium; and weighting the relative contribution of 1000s of DAS channels with far fewer conventional seismometer measurements. As we detail the method and its performance, we also identify and discuss remaining challenges of using fibreoptic datasets for earthquake detection.

2 THE EARTHQUAKE DETECTION RECIPE

2.1 Back-migration at a glance

The back-migration earthquake detection method converts continuous seismograms at each receiver into onset functions that represent the energy from a particular seismic phase arriving at

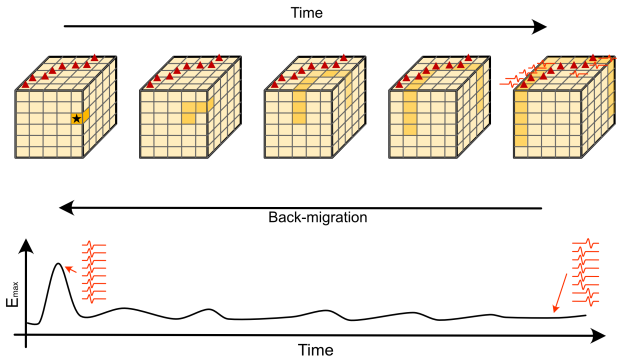

Figure 1. Schematic of back-migration of energy in space through time. Top shows the 3D volume at different points in time, with darker shading corresponding to higher back-migrated energy amplitude at particular grid cells. Red triangles denote receivers and black star denotes location of peak back-migrated energy, corresponding to a hypothetical earthquake. Bottom shows energy corresponding to a maximum amplitude grid cell at each point in time. As energy is back-migrated through the grid in time, the energy coalesces towards a singularity in space.

each receiver through time [Drew et al., 2013]. These characteristic onset functions from all receivers are then back-migrated in space through time, effectively stacking the data with physically-meaningful time-shifts. Potential events are detected by identifying coalescence peaks in the back-migrated energy through time (see Figure 1). The key strength of this method lies in events only being triggered by coherent source singularities rather than incoherent noise.

2.2 The QuakeMigrate algorithm

The specific back-migration algorithm used in this work is a modified version of the open source software QuakeMigrate [Hudson et al., 2019, Smith et al., 2020, Winder et al., 2021]. The specific steps of the modified QuakeMigrate algorithm are summarised in Figure 2. First, 3D travel-time and fibre-sensitivity lookup tables are generated for each receiver and each seismic phase (e.g. P, S), corresponding to the time-shifts required to back-migrate the characteristic onset function to a particular point in space. This computationally expensive step is only performed once for a given network and velocity model. One should note that this requires a velocity model, which theoretically limits the universal applicability of the method. However, typically one can make an approximate yet sufficient guess at an initial model. Second, continuous seismograms are read in for every receiver. Characteristic onset functions representing the energy arriving at each receiver are calculated, for example by using an STA/LTA ratio. Typically for conventional three-component seismic data, vertical components are used for P wave arrivals and horizontal components for S wave arrivals, although this obviously differs for DAS data (see Section 2.3). These characteristic onset functions are shifted and stacked in time for each point in the 3D search space, for all seismic phases (e.g. P and S). For each point in time, the value of the grid cell with the maximum coalescence of energy is recorded, producing a maximum coalescence time-series. The third step is to trigger possible event detections based on finding peaks in the coalescence time-series. Typically, we find the best trigger threshold is dynamic, using a multiple of the Median Absolute Deviation (MAD) value from a moving window of several hours in duration. Finally, one refines the event location by repeating the back-migration for each triggered candidate event individually. Event location can be refined by using data at a higher sampling-rate, a more spatially-dense lookup table, or different frequency filters, for example.

The outputs are an event catalogue, including arrival time picks for each seismic phase at each receiver, the earthquake origin time, and an estimate of earthquake location. Uncertainties are quantified for all parameters. Arrival time uncertainties are defined as the standard deviation of a Gaussian fit to the characteristic onset function for a given receiver and phase. Similarly, the earthquake origin time uncertainty is approximated as the standard deviation in time of the peak coalescence function. The earthquake location uncertainty is estimated from the standard deviation of a Gaussian fit to the marginalised coalescence in space at the earthquake origin time, which is assumed be a proxy for the probability density function in space. If desired, one can also output additional information such as plots of the coalescence in space and time or plots of arrival time pick labelled waveform data. These are useful for initial refinement of the detection parameters for a particular dataset, especially regarding STA/LTA values, bandpass filters and lookup table grid resolution.

2.3 Fibreoptic-specific modifications

Although back-migration earthquake detection methods already exist, a number of modifications are required to include fibreoptic datasets and optimise the algorithm. Modifications include com-

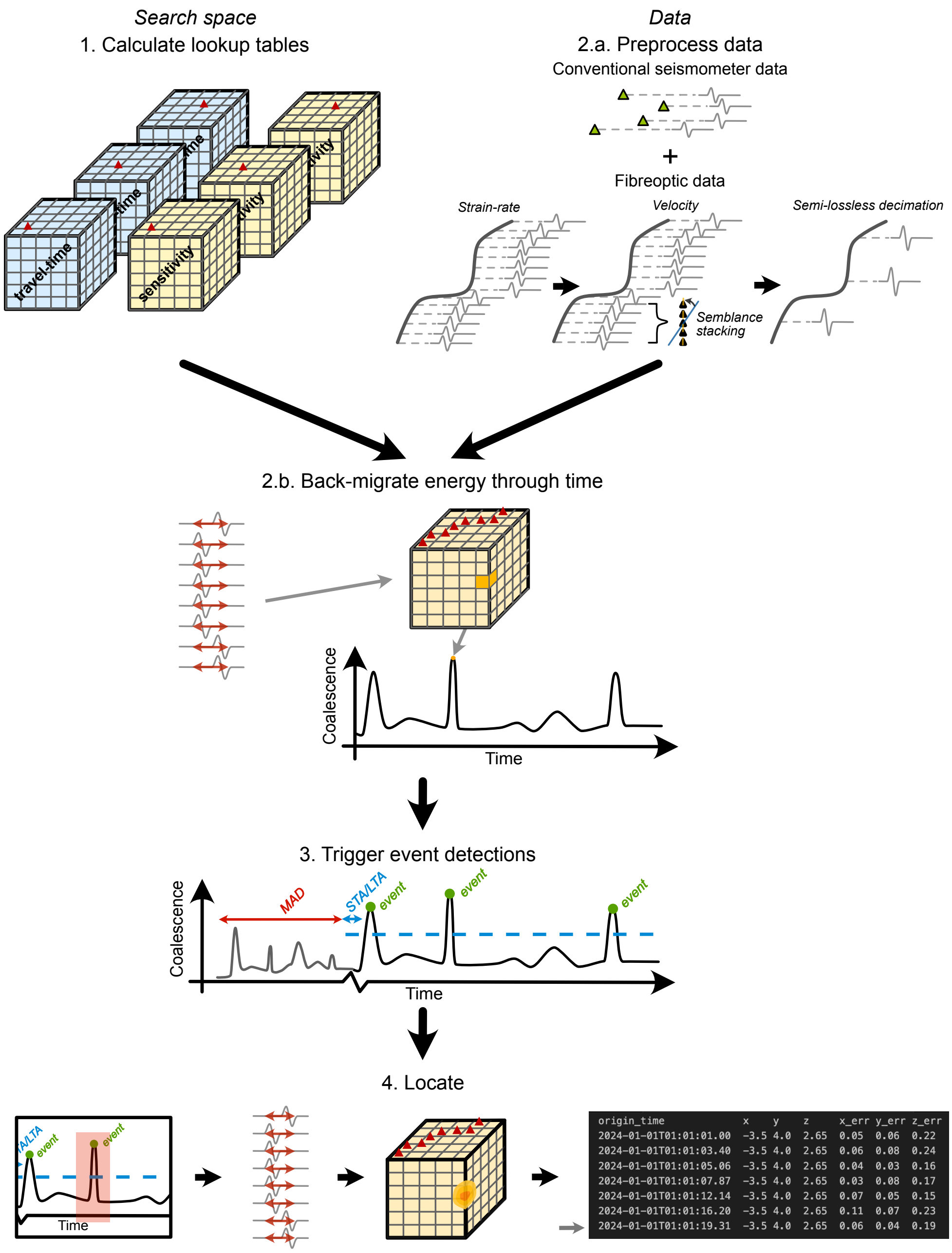

Figure 2. Overview of the modified back-migration detection method. 1. Travel-time and DAS sensitivity lookup tables calculated for each channel. 2.a. Data is preprocessed, including conversion and stacking of DAS data. 2.b. Onset functions are calculated and back-migrated through time. 3. Potential events are triggered from peaks in the time-shifted, stacked onset functions (corresponding to coalescence (or a measure of energy)). 4. Back-migration is performed again, just for candidate events. Uncertainties are estimated in this step and a final earthquake catalogue is generated.

bining datasets with different units (velocity, strain/strain-rate), lossless spatial decimation of DAS channels, considering fibre-medium coupling effects, accounting for in-axis fibre sensitivity, and both incoherent and coherent noise reduction via spatio-temporal filtering. All modifications are implemented into the QuakeMigrate algorithm. Below, we describe how these modifications are implemented, organised in relation to the aforementioned key earthquake detection ingredients.

2.3.1 Maximising spatial sampling extent and density

Including fibreoptic data for earthquake detection is an obvious way to enhance spatial sampling density. However, as we show in the results, enhancing spatial sampling density alone does not necessarily equate to enhanced earthquake detection performance. Where receivers are placed geographically may be of similar importance as number of receivers deployed [Strutz and Curtis, 2024, Toledo et al., 2020]. Fibreoptic deployments fall into two categories: fibreoptic cables deployed specifically for a seismological application versus interrogation of existing dark-fibre telecommunication networks. While the first category allows one to design an optimal network geometry, one has no influence of the geometry for the second category. Fibreoptic geometries can severely limit back-migration-based detection methods (e.g. it is impossible to uniquely back-migrate energy from a linear fibre geometry). Overcoming such issues is only possible by including other data, for example conventional seismometers, which will enhance spatial coverage in almost any scenario.

However, combining data from different instrument types is non-trivial. Fibreoptic interrogators measure strain-rate (or strain) whereas seismometers typically measure velocity. Strain-rate, $\dot{\varepsilon}$, is the spatial derivative of velocity, v. One might assume that we are ambivalent to receiver units, since we back-migrate an approximation of the normalised energy arriving at each receiver through time. However, spatially or temporally differentiating or integrating a periodic time-series leads to a systematic change in frequency-amplitude content. For example, let us assume that an earthquake has a simple sinusoidal signal,

$$v = \sin\left(\mathbf{k} \cdot \mathbf{x} - \omega \mathbf{t}\right),$$

where $\mathbf{k}$ is the wave number, $\mathbf{x}$ is the direction vector, ω is angular frequency and t is time. Then conversion to $\dot{\varepsilon}$ gives,

$$\dot{\varepsilon} = \frac{\partial v}{\partial x} = k.\sin\left(\mathbf{k} \cdot \mathbf{x} - \omega\mathbf{t}\right).$$

Since $k = 1/\lambda$, where λ is the wavelength, and the wavelength is proportional to the frequency (since $c = \lambda f$), the amplitude of $\dot{\varepsilon}$ is dependent on frequency. Such a relative change in frequency content in seismograms from different receivers could cause issues when pre-processing data inputs (e.g. bandpass filtering), and affect onset function amplitudes and hence overall coalescence amplitudes.

We therefore opt for converting all data into the same units before calculating and back-migrating onset functions if possible. An example of conversion from strain-rate to velocity is shown in Figure 3. This is only possible over approximately linear sections of fibre. If the fibre does not have significant sections that fulfil this criteria then we leave the data in native strain-rate. We choose to convert DAS strain-rate to velocity rather than converting seismometer velocity to strain-rate for several reasons. Firstly, converting seismometer velocities into strain-rate is highly challenging as one would have to combine all seismometer data, reconstruct the wavefield, and then take the spatial derivative of that wavefield at seismometer locations [Muir and Zhan, 2022]. This is impossible unless one has many conventional receivers. Secondly, integrating DAS strain-rate to velocity is not only more practical, but the resultant integration noise has infinite apparent velocity that can be removed using an fk-filter, increasing SNR. Thirdly, the integration also acts as a spatial low-pass filter, removing some incoherent noise. Fourthly, strain-rate is inherently more sensitive to local velocity structure than velocity [Capdeville and Sladen, 2024], with conversion to velocity removing this sensitivity. If an earthquake is far from the receiver and one does not know the local velocity structure adequately, then again one gains an improvement in back-migration performance. As we have already hinted, we convert from strain-rate to velocity via direct integration followed by an fk-filter to remove near-infinite apparent velocities.

In summary, maximising spatial coverage requires using data from as many receivers as possible. Back-migration algorithm performance is then improved by converting all data into the same

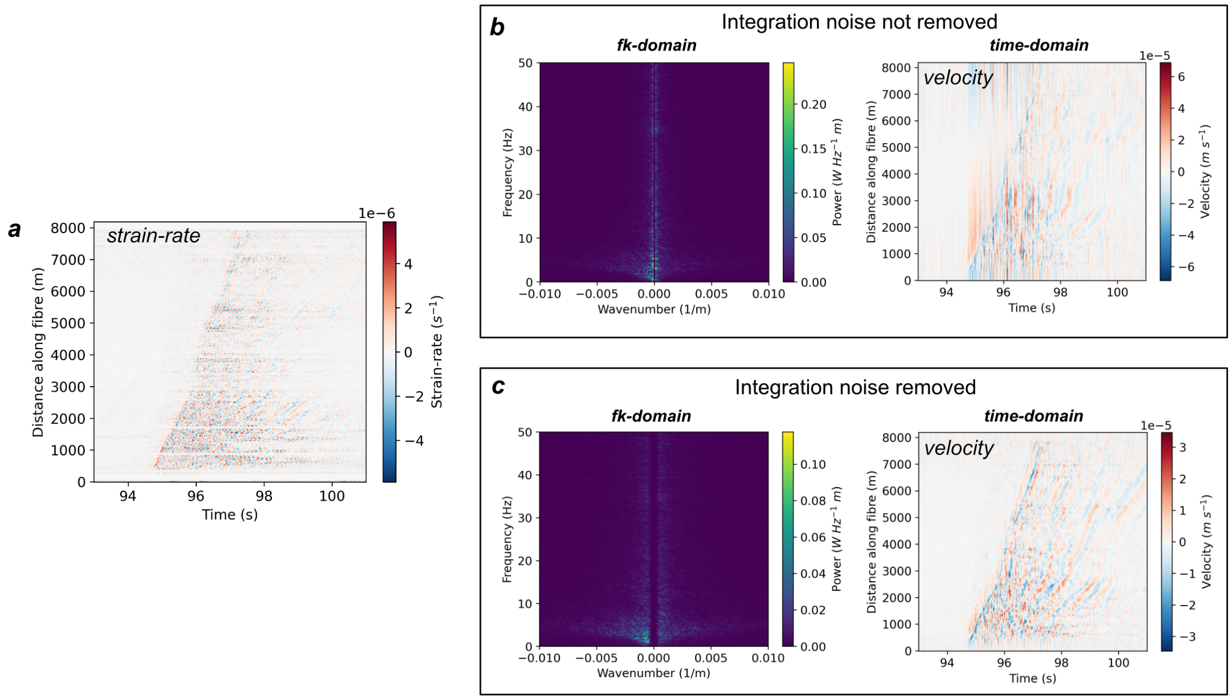

Figure 3. Example of strain-rate to velocity conversion. a. An earthquake distance along fibre vs. time plot for an earthquake from the Reykjanes Peninsula, Iceland in units of strain-rate. b. The same earthquake as in (a), but converted to velocity without removing infinite apparent velocity integration noise, both in fk-space and distance-time space. c. Same as (b) but with integration noise removed.

units (velocity), which both homogenises frequency content as well as reducing noise and heterogeneous local velocity structure effects.

2.3.2 Exploit signal coherency

The back-migration method inherently exploits coherency, which introduces both benefits and challenges when including fibreoptic datasets.

One benefit of exploiting coherency is associated with coupling of fibre to the medium. Ideally, one would quantify coupling and remove poorly-coupled channels from any analysis. However, quantifying coupling in fibreoptic deployments remains challenging. Instead, here we simply capitalise on the assumption that poor coupling results in incoherent noise that cannot be back-migrated. Poorly coupled channels will reduce the overall maximum theoretical coalescence value, since the channels may not contribute but crucially poor coupling will not contribute to false triggers.

The primary challenge associated with including fibreoptic data is the large number of channels compared to conventional receivers. The challenge lies in how to balance information from typically lower SNR, single-component fibre channels and higher SNR conventional seismometer data. This is not an issue if using only fibreoptic data. However, in the most extreme case one might have many (n) fibreoptic receivers and a single seismometer receiver. Theoretically one could assign receiver types different weights, but such weighting is limited because as one preferentially weights data from one receiver, it also preferentially weights noise. Hypothetically if one equally weighted a single seismometer with the same weight as n fibre channels, seismometer receiver noise would contribute n times that of noise on a single DAS channel. This would potentially negate any coherency gain.

We instead opt for weighting the contribution of fibreoptic receivers relative to conventional instrumentation via semi-lossless decimation. This semi-lossless decimation refers to performing semblance-based stacking on every n fibreoptic receivers, similar to Porras et al. [2024]. Specifically, semblance-stacking comprises time-shifting every channel relative to every other channel in order to maximise the stacked amplitude. Time-shifts are limited by a maximum permissible apparent velocity. Theoretically this preserves both amplitude and directional information. However, we refer to the method as semi-lossless rather than lossless as we discard the directional information but preserve coherency post decimation. This semblance-based decimation improves decimated fibreoptic receiver signal quality, which at some point would theoretically have sufficiently high SNR to provide equal constraint/information in the detection algorithm to any conventional receivers. Weighting therefore remains subjective, controlled by the number of DAS channels stacked. In practice, one is limited by the fibre geometry, since semblance-based stacking does not work on arbitrary orientations of fibre (e.g. it would fail if applied to two channels orthogonal to one another). Therefore, in practice we currently employ the philosophy of decimating as much as possible while preserving both semblance-stack performance (e.g. only over linear segment scales or the gauge-length) and spatial coverage.

2.3.3 Maximise sensitivity to multiple seismic phases

A strength of back-migration detection methods is that one can use multiple seismic phases to constrain earthquake location better, enhancing coalescence and therefore improving detection performance. QuakeMigrate traditionally does this for P- and S- waves by back-migrating vertical and horizontal receiver component onset functions through P-wave and S-wave velocity models, respectively. Fibreoptic channels only measure signals in the fibre axis, making it non-trivial to isolate different seismic phases. Instead, we modify the algorithm to allow one to use fibreoptic channels for both P and/or S phases, as well as surface waves. This can be specified wholesale or individually for every channel, depending on whether a channel is horizontally deployed on the surface or vertically in a borehole, for example. Currently, the surface wave implementation involves specifying a single group velocity for the medium and assuming the energy migrates within the near-surface. However, more rigorous inclusion of surface waves could be achieved by modifying the method to back-migrate energy through different phase-velocity models for different frequency bands, approximately simulating surface wave dispersion and Rayleigh vs. Love waves.

Above, we hint that fibre channel orientation and surface vs. subsurface deployment play a role in the sensitivity of a particular channel to a particular seismic phase. While this topic could be the subject of numerous studies, one can typically assume that subsurface channels deployed vertically are sensitive to both P and S waves, whereas horizontal surface channels are dominantly sensitive to S-waves because of steep near-surface velocity gradients resulting in near-vertical ray incident angles [Hudson et al., 2021]. An exception to this is if the medium has an approximately homogeneous velocity structure, for example if deployed on ice [Walter et al., 2020]. However, for the surface DAS examples in this work, one has a homogeneous velocity structure and so has similar sensitivity for both P and S waves, and although the other is dominantly sensitive to S-waves, we still observe some P-wave energy in that case too.

In reality, the sensitivity of fibreoptic cables to different seismic waves is not binary. A more sophisticated approach that we implement here is to calculate fibreoptic channel sensitivity based on ray takeoff angle derived from the same velocity model used to calculate travel-time lookup tables. We calculate the takeoff angle for a ray propagating to each receiver from every grid cell in the search volume, for both P and S waves. Fibreoptic sensitivity to strain-rate and velocity differ, so for flexibility we implement both. For velocity as measured by fibreoptic channels, the sensitivity of a fibreoptic channel to P, SV and SH phases is given by [Martin, 2018],

$$\zeta_P = \cos(\phi_1 - \theta)\cos(\phi_2),$$

$$\zeta_{SV} = \cos(\phi_1 - \theta)\sin(\phi_2),$$

$$\zeta_{SH} = \sin(\phi_1 - \theta),$$

where θ is the angle of the fibre on a plane relative to a reference direction (e.g. north), ϕ_1 is the in-plane angle of a plane wave propagation direction relative to the same reference direction, and ϕ_2 is the angle of the plane wave relative to the plane-perpendicular angle (e.g. angle from vertical down for a horizontal fibre channel). Alternatively, for strain-rate the sensitivity is,

$$\zeta_P = \cos^2(\phi_1 - \theta)\cos^2(\phi_2),$$

$$\zeta_{SV} = \cos^2(\phi_1 - \theta)\sin(2\phi_2),$$

$$\zeta_{SH} = \sin(2(\phi_1 - \theta))\cos(\phi_2).$$

Note that these are for point strain and we drop any wave amplitude factors and frequency or phase dependence since we do not know the amplitude, frequency content or phase of any prospective arrivals prior to detecting them. SV and SH sensitivities then have to be somehow combined. Since the proportion of SV to SH energy incident at a receiver prior to detection is unknown, maximum sensitivity to any given S-wave polarisation is assumed. We therefore define the S wave sensitivity as,

$$\zeta_S = max\left(\sqrt{\frac{\zeta_{SV}^2 + \zeta_{SH}^2}{2}}, \zeta_{SV}, \zeta_{SH}\right).$$

These equations are now implemented in QuakeMigrate. We then define a sensitivity threshold below which we deem that a particular fibre channel is insensitive to that location within the search volume. Such a threshold could be selected, for example, by determining at what sensitivity value the amplitude of a fibre channel would fall below the noise level of another channel with perfect sensitivity. We then mask these regions for the associated seismic phase at that particular channel. We do this for all fibreoptic channels. This provides greater constraint over where potential events coalesce. This approach is dependent on knowledge of the approximate velocity structure, especially the shallow velocity gradient. It should therefore be used with caution, with the user able to choose whether to implement it or not. While it is computationally intensive, it is only performed once when the travel-time lookup tables are generated, so subsequent runtime on continuous seismic data is unaffected.

While we only address body-wave sensitivity here, theoretically, one can also surface wave sensitivity in a similar way.

2.3.4 Quantify uncertainty

No explicit uncertainty quantification modifications are made to the QuakeMigrate back-propagation method. However, several modifications will affect uncertainty estimates. Arrival time uncertainty estimates for fibreoptic receivers will depend on the number of channels stacked, with stacking improving the SNR, but potentially reducing the first break resolution. Applying semblance-stacking minimises this issue by time-shifting each trace so that first breaks should be aligned. Here, we typically perform semblance stacking on upsampled data ($\times 10$), preserving time precision. Including fibreoptic data also affects hypocentre uncertainty estimation. Dense fibreoptic channel spacing (typically order of metres) may be far smaller than the size of the grid cells in travel-time lookup tables, which means that these fibreoptic channels may not optimally contribute to hypocentre constraints and hence not minimise uncertainty. Furthermore, using fibreoptic channel sensitivity to mask out regions of the search space could change hypocentre uncertainty estimates, either reducing uncertainty if the velocity model structure used to calculate sensitivity is sufficiently close to the true structure, or artificially perturbing the uncertainty if not.

2.3.5 Maximise computational efficiency

Back-migration detection methods are inherently computationally expensive compared to simpler, receiver-by-receiver detection methods. However, QuakeMigrate runs in approximately real-time for the experiments presented here (using 8 processors on an Apple M3 Pro CPU). These efficiencies are primarily driven by three contributions: computing lookup tables only once for entire datasets; reading in continuous seismic data in blocks rather than entire files, minimising read-write operations; and implementing the core back-migration step in the pre-compiled C language. To minimise the additional computational expense of including fibreoptic data, we only compute sensitivity lookup tables once, and perform lookup table masking without the need to subsequently store sensitivity information independently in memory. Secondly, we support reading of a number of native DAS data formats (hdf5, segy etc) directly, which are typically split into small, one minute duration files. One can then simply run QuakeMigrate over minute long time-windows, optimising costly read-write processes and memory usage.

3 DATA

Three datasets are used to investigate performance of the new method. These datasets approximately represent end-members of current fibreoptic deployments: (1) a dense 2D fibreoptic grid deployed coincident with nodes on a glacier; (2) a dark-fibre located within the vicinity of a volcanic eruption; and (3) a downhole fibre at a geothermal field. The specific detection algorithm settings used in each case are given in Table 1.

The glacier dataset comprises of 1.2 km fibre deployed at Gornergletscher in the Swiss Alps, in October 2023. The network has a ~ 100 m aperture, with 29 single vertical component Sercel WiNG nodes deployed in the same area. The interrogator used is a Sintela Onyx, measuring strain, with a gauge-length of 6 m and a channel spacing of 1.6 m. All data were acquired with a sampling rate of 1000 Hz. The majority of microseismicity at the study site is thought to be caused by near-surface crevassing [Walter et al., 2009, Hudson et al., 2020].

The volcanic eruption dataset comprises of an 8 km dark fibre, interrogated during the first Svartsengi volcanic eruption on the Reykjanes Peninsula, Iceland, in December 2023. We also include data from a broadband seismometer operated by the Icelandic Meteorological Office. The fibreoptic interrogator used is a Silixa iDAS, measuring strain-rate, with a gauge-length of 10 m and a channel spacing of 16 m. All data are sampled at 100 Hz. Seismicity detected here is attributed to one intrusion episode on the 18^{th} December 2023.

The downhole geothermal dataset is from the Utah Frontier Observatory for Research in

Table 1. QuakeMigrate detection settings for each dataset in this study.

Parameter	Glacier	Volcanic eruption	Geothermal borehole
Phases used	P, surface	P, S	P, S
Sampling rate	1000 Hz	100 Hz	1000 Hz
Frequency filter, P	10-250 Hz	1.2-20 Hz	2-300 Hz
Frequency filter, S	n/a	1.2-20 Hz	2-300 Hz
Frequency filter, surface	5-150 Hz	n/a	n/a
Grid resolution, x	8 m	150 m	400 m
Grid resolution, y	8 m	150 m	400 m
Grid resolution, z	10 m	300 m	100 m
STA/LTA P	0.01/0.2	0.2/1	0.01/0.5
STA/LTA S	0.02/0.2	0.2/1	0.01/0.5
Coalescence detection threshold	1.15	1.125	1.7
Marginal window	0.25 s	2 s	0.25 s
DAS specific settings			
Spatial downsamp. factor	1	5	10
Channel spacing	1.6 m	16 m	1 m
Gauge-length	6.38 m	10 m	10 m
Semblance-stacking	no	yes	yes

Geothermal Energy (FORGE) 2019 experiment, consisting of 1.2 km of fibre cemented into a vertical monitoring borehole [Lellouch et al., 2020]. A network of seismometers was deployed at the surface. The fibre is interrogated using a Silixa iDAS interrogator with a gauge length of 10 m, a channel spacing of 1 m and a sampling rate of 100 Hz. Here, we focus on one particularly active hour of seismicity during a well stimulation at 17:00 to 18:00 on 27 April 2019.

While these example datasets are not comprehensive, the majority of fibreoptic deployments for studying seismicity are likely similar to at least one of these examples, perhaps with the exception of subsea and urban deployments.

4 RESULTS

4.1 Algorithm performance

Before showing earthquake catalogues for each example dataset, we first investigate various specific aspects of the detection algorithm performance in more detail. In particular, we focus on the importance of spatial coverage when including both fibreoptics and seismometers, stacking fibreoptic channels, fibreoptic coupling, and fibreoptic sensitivity.

4.1.1 Spatial coverage and fibreoptics-only vs. combined fibreoptics and seismometers

Adequate source localisation is essential for any back-migration detection method, such as the one described in this study. Theoretically, the better the source localisation, the higher the peak energy observed in the space-time search space and hence the more likely an event is to be detected above the ambient noise level. Figure 4 exemplifies how important spatial extent of sampling of the seismic wavefield is for source localisation and hence detection. Here, P and surface waves are used to detect an example icequake. Figure 4a shows the example earthquake detected by QuakeMigrate using only two vertices of the Gornergletscher fibre. Such a geometry is typical of many fibre deployments, for example that of the Iceland volcanic eruption dataset in this study. The dashed line in Figure 4a shows the 95% contour of the peak coalescence, with the blue star indicating the location of the peak corresponding to the inferred icequake location. The result of Figure 4a can be compared to that of Figure 4b, where the whole 2D fibre is used to detect and locate the same icequake. The icequake hypocentre moves considerably, with no overlap in the 95% contours for the two solutions. When one also includes the 29 nodes in the detection (Figure 4c) then although the icequake hypocentre moves again, this time it is within the 95% contour. The additional constraint provided by the nodes further constrains event location and hence the ability to detect the event above the noise level. The results of Figure 4 show how important maximising spatial sampling coverage is for source localisation and hence detection. For glacier deployments, it is conceivable to deploy dense 2D geometries, but in other situations it is likely that maximising spatial coverage will often require the combination of conventional seismometers and/or nodes in addition to fibre.

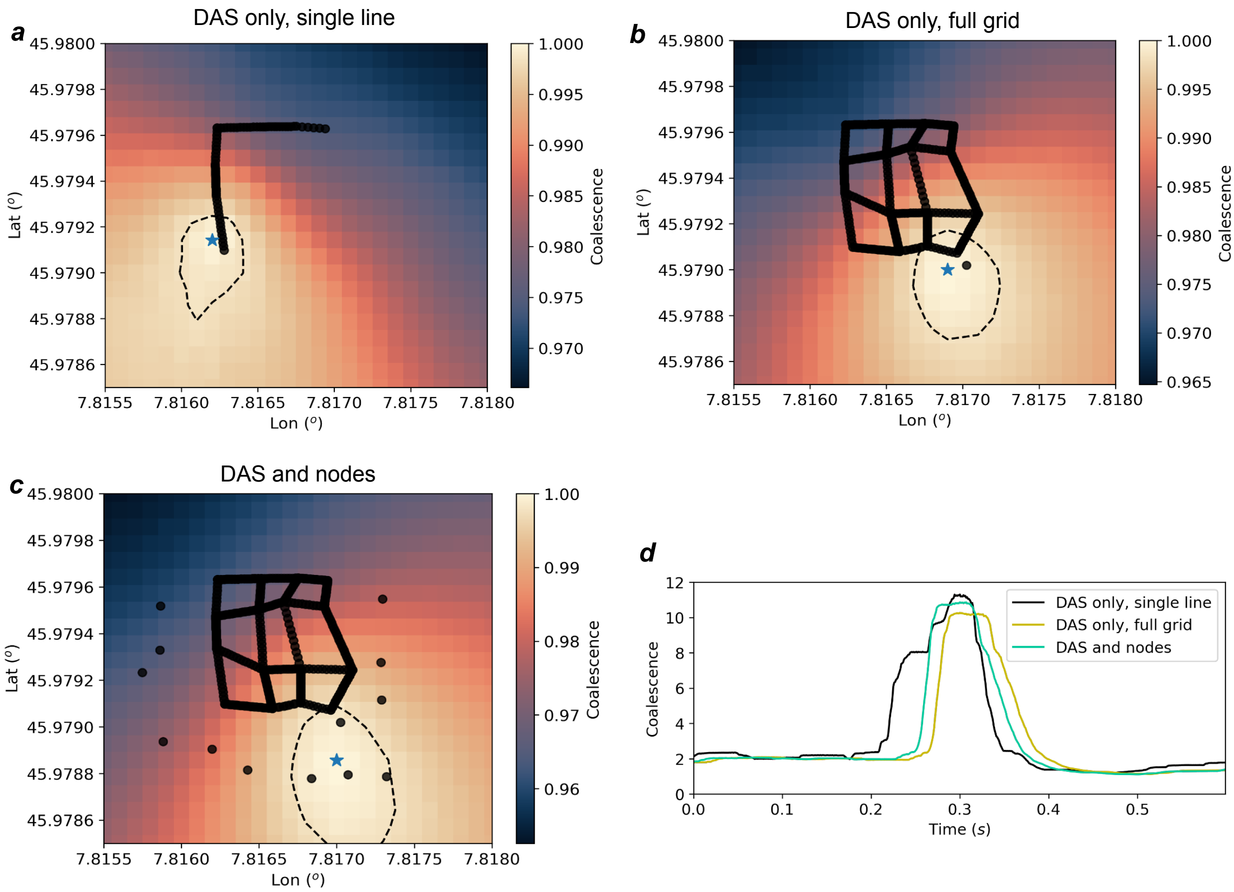

Figure 4. Example of how important spatial coverage is for back-migration earthquake detection. Data shown is from an icequake at Gornergletscher, Switzerland. a. Map view of the 3D coalescence space at the earthquake depth and origin time, for a simple fibre geometry consisting of only two vertices of the entire fibre deployment, typical of many current or dark fibre deployments. Blue star indicates the peak coalescence corresponding to the inferred icequake hypocentre. Black dashed line indicates the corresponding 95% contour. b. Same as (a) but using all fibre channels to detect the icequake. c. Same as (a,b) but also including the co-deployed vertical single-component nodes. d. Comparison of maximum single-pixel coalescence values through time for each setup in (a) to (c).

4.1.2 Stacking and coupling

Two immediate challenges of processing fibreoptic datasets are processing large data volumes resulting from inherently dense spatial sampling and fibre-medium coupling issues. Figure 5 summarises the effects of stacking fibre channels to reduce data volumes and accounting for coupling effects by removing poorly coupled channels, for the glacier dataset.

The effect of stacking multiple fibre channels is shown in Figure 5b. The motivation for stacking is two-fold: firstly to reduce data volumes and hence increase computational efficiency; and secondly to move towards balancing contributions from fibre channels and seismometers/nodes. The result in Figure 5b applies semblance-stacking to every 10 channels (16 m), aiming to preserve spatio-temporal coherency information while spatially downsampling the data. The results show that downsampling the fibre via stacking does not have a significant effect on the hypocentral location but does result in a spatially more constrained peak in the coalescence. This result is interesting since it shows that the semblance-stacking not only preserves the coherency information but acts to reduce noise effects between individual channels, enhancing the overall coherency of the solution in space and hence improving detection performance. Semblance-stacking therefore not only gives a computational performance gain (both in terms of efficiency and memory usage), but also enhances detection algorithm performance, at least in this instance.

The effect of removing poorly coupled channels on detection performance is shown in Figure 5c. Here, we remove channels that traverse crevasses and are hence poorly coupled to the ice and comparatively well coupled to the atmosphere. Not only are these channels therefore approximately insensitive to subsurface seismic energy, but actually have higher noise amplitudes due to atmospheric effects such as wind, for example. The results are remarkably similar to those of Figure 5b, with no distinguishable difference in the location of the coalescence peak, but the 95% contour becoming better constrained spatially. One might expect removing poorly coupled channels to have a greater effect. However, we attribute the relatively insignificant change in performance to be a result of a key strength of back-migration, in that poorly-coupled channels represent incoherent noise that theoretically should not contribute significantly to event detection. At least in this example, accounting for coupling appears to not be of first-order importance.

4.1.3 Including fibreoptic sensitivity

The influence of accounting for the effects of fibreoptic measurement sensitivity are shown in Figure 6 for both a glacier icequake (Figure 6a-d) and a volcano-tectonic earthquake (Figure 6e-i). For the glacier icequake, accounting for sensitivity affects the coalescence, including both the peak and extent of the 95% contour, moving the peak and tightening the spatial constraint (see Figure 6b

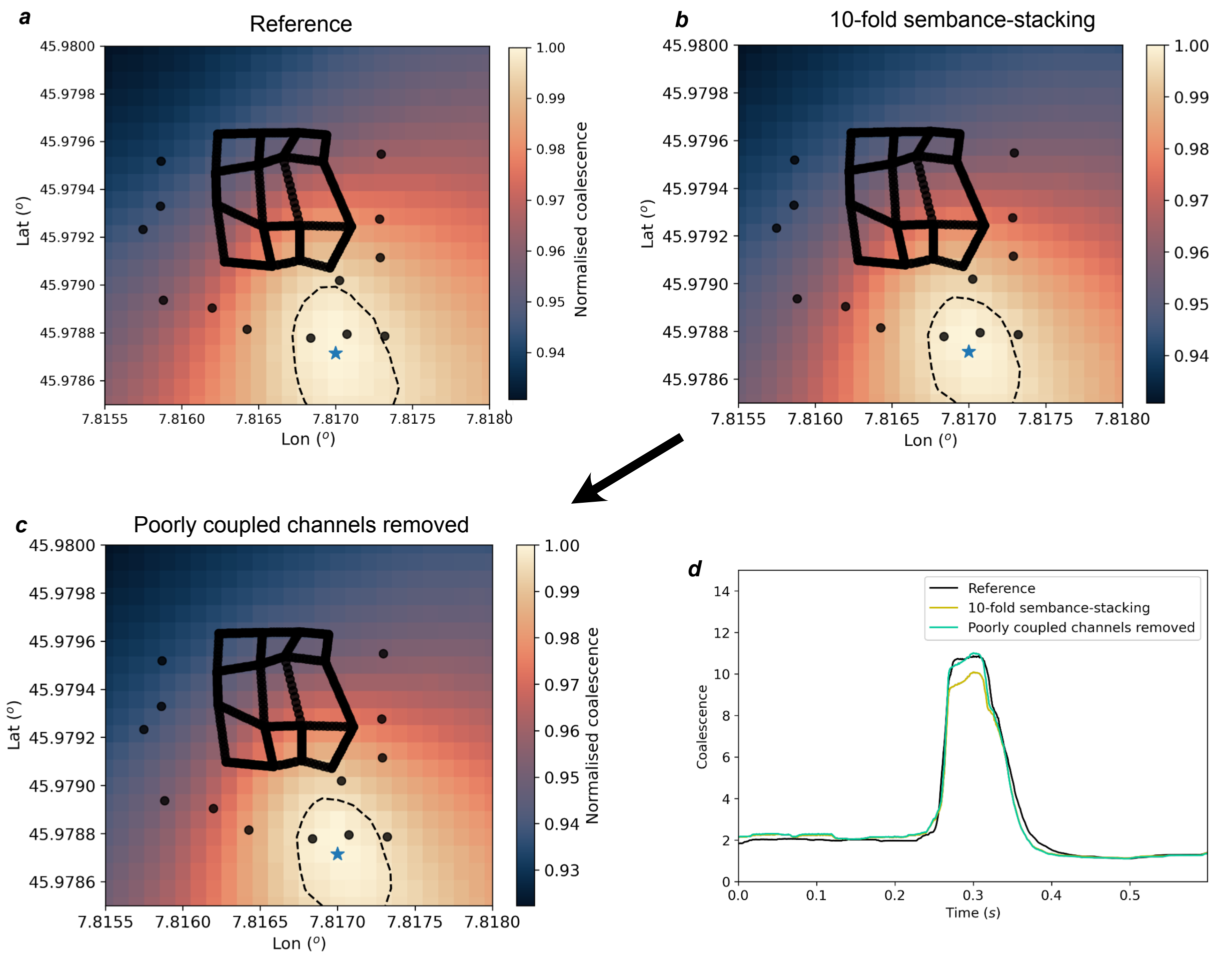

Figure 5. Effect of stacking and coupling on detection algorithm performance. a. Reference coalescence map, using all available fibre channels for detection of an example icequake. b. 10-fold (10 channel) semblance-stacking result for the same icequake as in (a). c. Detection result for same icequake as in (a) except with poorly coupled channels removed. d. Comparison of maximum single-pixel coalescence values through time for each setup in (a) to (c).

vs. Figure 6a). The effect is more extreme than the effects of stacking or removing poorly coupled channels (Figure 5). Accounting for sensitivity for the volcanic earthquake example has a smaller effect. This is despite the geometry being far more linear than in the icequake example. While the 95% contour encloses a smaller spatial extent, the earthquake hypocentre moves only ~ 100 m, relative to the 8 km fibre. We attribute this behaviour to the fact that the somewhat linear fibre geometry here has a highly non-uniform sensitivity to both P and S waves, and so the network is only sensitive to seismic energy from these regions already, so the additional sensitivity constraint we impose has little effect. This is contrary to the icequake example, where the overall network has an approximately homogeneous sensitivity to incoming energy from any source location. We argue that it is therefore debatable whether one should impose any sensitivity constraint in practice, since it is already incorporated into the analysis and if the velocity structure is poorly constrained then the sensitivity maps will also be poorly constrained. However, in any case, plotting up the sensitivity maps for various seismic waves (Figure 6c,g,h) is insightful and should always be compared to the distribution of earthquake hypocentres output from a detection and location algorithm.

4.2 Generating earthquake catalogues

4.2.1 Glacier

Figure 7 shows the icequake catalogue from the fibreoptic deployment at Gornergletscher in the Swiss Alps. The majority of these icequakes are likely generated by near-surface crevassing [Walter et al., 2009, Hudson et al., 2020]. Firstly, the 2D fibre geometry results in no apparent bias in the spatial distribution of seismicity. In this example, we use both P- and surface- waves to contribute to event detection. The surface fibre deployment is sensitive to P-waves due to the approximately homogeneous velocity structure of ice, with no shallow slow velocity firn layer present. Such slow velocity layers at glaciers have proven problematic for P-wave detection previously [Hudson et al., 2021]. S-wave energy generated by crevassing is expected to be minimal [Hudson et al., 2020], so is not used here. Since the ice column is assumed to be of < 100 m thickness and the dominant icequake generation mechanism is expected to be near-surface crevassing, we also use surface-waves for detection. The site has several sources of noise, including wind and subsurface fluids that flow through some of the fractures. Coupling directly to glacier ice in such conditions can be challenging, but in this experiment the fibre is generally well-coupled to the ice since the fibre froze in within the first 12 hours of the deployment. The quality of coupling can be seen in Figure 7b, with most channels showing clear P- and surface- wave arrivals for an icequake, but with a number of channels showing only noise where they are suspended above a crevasse (at ~ 470 m, ~ 750 m and ~ 970 m, for example). Here, all channels are included for detection. This is based on the finding that the algorithm is unaffected, at least to first-order, by poorly coupled channels with spatially uncorrelated noise (see Figure 5c).

173 icequakes are detected in six hours. While there are likely more icequakes in the dataset, we opt to lower the detection threshold only to a point where we are confident that we minimise false detections. Figure 7b-d shows results for one icequake. The detection algorithm generally picks both P- and surface- wave first breaks where one would manually identify them, after accounting for uncertainty, although uncertainties are large (of the order of the dominant surface-wave period). Seismic energy arriving at one of the nodes is also shown in Figure 7d, evidencing that the detection algorithm performs adequately on both conventional and fibreoptic data in combination, one of the key aims of this work.

4.2.2 Volcanic eruption

Figure 8 shows an earthquake catalogue during one episode of the ongoing Sundhnúkagígar eruption, Iceland. The dark fibre interrogated during this experiment has a somewhat linear geometry, typical of many dark fibre geometries, following a road from a geothermal power plant to the coast. Both the geothermal plant (at the fibre origin) and the coast (at the far end of the fibre) generate coherent noise. Coherent noise sources can affect the performance of the detection algorithm if they contain energy within the bandwidth of interest. These noise sources detrimentally affect phase arrival identification from 0 m to 300 m and beyond 7900 m along the fibre. The presence of both natural and anthropogenic noise, along with the numerous earthquakes that occur over the time period make this dataset an ideal case study.

The fibreoptic data combined with a single seismometer detects 886 earthquakes within the region shown in Figure 8a on the 18^{th} December 2023, compared to 826 earthquakes detected within the same region by the permanent regional monitoring network (operated by the Icelandic Met Office). However, although the energy from the earthquakes coalesces sufficiently to make detections, the locations typically remain poor. We expect the majority of seismicity to align with the opening rift [Sigmundsson et al., 2024], but instead find that the seismicity clusters near one end of the fibre. This is likely for several reasons. Firstly, many of the earthquakes detected are close to the noise level, affecting the accuracy of individual channel arrival time picks. Secondly, and likely more significantly, the geometry of the fibre provides poor location constraint (see Figure

6c,d). This is partly due to poor azimuthal coverage but also likely the result of low sensitivity to P-waves from certain regions of the seismically active rift. Poor azimuthal constraint likely results in poor locations, primarily because the regional velocity model used is likely faster than the true shallow velocity structure.

Even though locations are poorly constrained, phase arrival times for some events are promising. For example, the earthquake shown in Figure 6b-d shows P and S arrival time picks close to the first break, with realistic uncertainties, even though the P-wave amplitude is close to the noise level. This is particularly clear in Figure 6c. It is surprising that one can even observe P-waves on the fibre at all, given the crustal setting. However, we attribute this to be due to the fibre being deployed within metres of the bedrock, removing much of the effect of a steeply varying near surface velocity gradient that would otherwise refract P-waves towards vertical incidence. The earthquake arriving at a conventional seismometer also included for detection is shown in Figure 6d, again confirming the promising performance when processing hybrid fibreoptic-seismometer datasets.

While it is encouraging that the detection algorithm works well even when locations are poorly constrained, our findings from this dataset illustrate the challenges associated with using fibreoptic data from dark fibres for source localisation.

4.2.3 Geothermal borehole

Figure 9 shows an earthquake catalogue for one hour during a stimulation test at the Utah FORGE experiment. The deployment is typical of many borehole DAS deployments, with only a vertical fibre cemented into a well, with seismometers deployed at the surface. For the hour of data we analyse, the closest surface seismometers to the injection well have too high noise to observe any subsurface seismicity. We therefore use only one seismometer, FORU, in combination with the downhole fibreoptic data.

We detect 135 earthquakes, compared to 125 earthquakes detected using a combination of standard methods and matched filter processing with a string of 12 borehole geophones [Dzubay et al., 2022]. Most earthquakes are present in both catalogues. One should note that comparing numbers of earthquake detections can be misleading, since one can lower detection thresholds and detect many more earthquakes or vice versa. Obviously one can check candidate events individually, but this is not feasible for datasets with ¿1000s earthquakes. Here, we try to avoid this by setting the detection threshold to a level where we minimise false detections while still detecting as many real events as possible. However, it is still worth emphasising that the detection algorithm of this study detects a comparable number of earthquakes to the most sensitive detection method possible, a matched filter method. Although there is no ground truth, we deem earthquake locations to be poor, with a portion of the earthquakes detected locating far from the stimulation well located at approximately 38.5^oN, 112.9^oW. Similar to the volcanic eruption example, we attribute poor location constraint to be dominantly caused by network geometry. If more surface instruments were usable, locations would likely be constrained better.

Although locations are interpreted to be poor, this does not translate to poor earthquake detections, consistent with our findings from the volcanic eruption results. This is demonstrated for the example earthquake shown in Figure 9b. Both P- and S- wave phases are identified with small uncertainties compared to the other datasets presented. This is likely due to a combination of good coupling of the cemented fibre, as well as perhaps lower noise levels in the subsurface and a relatively homogeneous velocity structure in the vicinity of the monitoring well. S-wave arrivals may be incorrectly identified in some cases (see Figure 9c), but this is to be expected given the noise levels and/or P-wave coda.

5 DISCUSSION

5.1 Practical considerations influencing earthquake detection with fibreoptic sensing

The findings of this work emphasise a number of practical considerations affecting earthquake detection using fibreoptic sensing. While we focus on local microseismicity detection using a back-migration method, most of the points below also hold for earthquake detection using fibreoptic sensing more generally.

(i) The spatial sampling extent of the seismic wavefield plays the most important role in earthquake localisation, yet back-migration based detection still performs successfully in practice, even if the coherent source of energy is poorly constrained spatially. Specifically, the geometry of the fibreoptic cable plays an important role, evidenced by the glacier 2D grid deployment of fibre detecting and locating events better than highly linear fibre geometries such as the volcanic eruption dataset, for example. Extrapolating from this, we expect 3D fibre geometries to further improve performance. In practice, many fibreoptic cable geometries are limited by practical constraints, and so combining fibreoptic data with conventional receivers provides an optimal alternative.

(ii) Fibreoptic sensing inherently provides dense sampling of the seismic wavefield. Decimation of this data is important for increasing the computational efficiency and minimising memory usage in practice. We find that using semblance-stacking [Porras et al., 2024] to decimate the data preserves wavefield coherency information. Such stacking is applicable where fibre geometries have linear sections at least of the order of the spatial decimation/stacking length.

(iii) Conversion from native strain or strain-rate to velocity enhances performance, for fibre geometries with substantial linear sections or low curvature. For example, we find a phase pick accuracy gain for the volcanic eruption example but not the glacier example. This gain is primarily attributed to dampening sensitivity to subsurface heterogeneities [Capdeville and Sladen, 2024] but also the isolation of integration noise.

(iv) Compensating for fibreoptic sensitivity can provide additional spatial constraint of coalescence peaks, but the benefit is limited. This finding is important because it implies that sensitivity may not be a major practical concern for earthquake detection for most deployments.

(v) There exists an optimal spatial resolution of the 3D search grid. We introduce this specific back-migration concept here, since it can play an important role in our detection algorithm performance. Specifically, too high a resolution grid results distributes coherent energy between more grid cells, due to velocity structure uncertainty, resulting in lower peaks in coalescence. Conversely, too low a resolution grid results in high coalescence values of a single grid, but risks not isolating coherent earthquake signals from coherent or even incoherent noise. Optimal grid cell resolutions for each example in this work are given in Table 1.

(vi) There also exists an optimal moving time-window with which to process the data. Again, this point is a specific back-migration concept, but important for users of the detection algorithm presented here. Specifically, the time-window over which one processes phase arrivals must be sufficiently long that the uncertainty in phase arrivals can be adequately estimated, while being sufficiently short to eliminate phase mis-association.

5.2 Comparison to alternative approaches

The greatest strength of fibreoptic sensing is the orders-of-magnitude denser spatial sampling over conventional instrumentation. Coherency-based back-migration methods such as that described in this study by definition capitalise on coherency between these densely sampled channels in a way that receiver-by-receiver detection methods cannot. Receiver-by-receiver STA/LTA algorithms are susceptible to triggering off incoherent noise. Receiver-by-receiver machine-learning-based phase arrival detection methods are theoretically less sensitive to incoherent noise since they approximately learn to identify the noise field, but this requires the availability of a training dataset of existing detected earthquakes. Furthermore, all receiver-by-receiver methods struggle with phase association. Although machine-learning derived phase associators exist [Ross et al., 2019b], we find that they do not always perform adequately for local seismicity (within 5 km of a network). The only benefit of receiver-by-receiver methods over back-migration is computational efficiency. However, the all the examples presented in this work run faster-than-real-time on a standard computer (8 processors on a Apple M3 Pro CPU). Surpassing the faster-than-real-time benchmark is key for any seismic monitoring application, with any additional gains only a bonus.

Some promising advances in detecting earthquakes using fibreoptics have been made by assessing coherent energy arriving at many fibre channels simultaneously. These include explicit methods such as assessing the curvature of arrivals on linear fibre using semblance methods [Porras et al., 2024], and implicit methods that use machine-learning image recognition algorithms [Stork et al., 2020, Huot et al., 2022] to identify similar features. Although these methods are promising, typically detecting events close to the noise-level, there are a number of limitations. Firstly, explicit semblance-based methods require specific, linear fibre geometries, or at least substantial lengths of linear fibre. It is unclear how sensitive machine-learning image recognition algorithms are to fibre geometry, but current implementations would have to be retrained for every new deployment or new fibre geometry. A further limitation is that it is challenging to conceive of ways to include both fibreoptic and conventional receivers in such detection frameworks. Huot et al. [2024] lay foundations for combining fibreoptic and conventional receivers in a machine learning algorithm by running two binary logistic regression models in parallel and identifying events detected by both. They find that this significantly reduces false triggers compared to only using the fibreoptic data, emphasising the importance of combining data from all available receivers where possible. However, unlike the back-migration method we present here, such methods do not yet fully couple the information provided by multiple receiver types, and therefore do not yet fully realise the associated performance gain.

5.3 Perpetual challenges

A number of challenges remain for using fibreoptics for earthquake detection. Particular challenges that are difficult or even impossible to overcome are as follows. Firstly, fibreoptic cables are sensitive only to in-axis strain. This limits sensitivity to multiple seismic phases, especially in the presence steeply varying shallow subsurface velocity gradients [Hudson et al., 2021]. Helically-wound fibre has the potential to overcome this issue [Baird, 2020], but still represents a pseudo-1D measurement, is costly, and is never deployed in telecommunications networks. Secondly, fibre-medium coupling remains generally both poorly constrained and for some experiments uncontrollable [Paitz et al., 2021]. Recent work allows one to quantify expected coupling response [Celli et al., 2024] and if a fibre is buried, frozen-in or cemented in-situ then coupling is approximately perfect. However, for fibres deployed on the surface or deployed in conduits, for example dark fibres, coupling is challenging to quantify. Thirdly, our results emphasise the importance of fibre geometries and spatial extent, yet at least for dark fibre deployments one has little or no control over the deployed geometry. Overcoming this issue may be possible by interrogating many fibres in dense, urban environments, but will remain a challenge in rural or subsea regions. Fourthly, data volumes remain challenging. Experiments can generate 100s GB to TBs of data per day. Downsampling data will therefore become essential with increasing deployment duration and/or increased deployment spatial scales. The semblance stacking component described in this study may allow on-the-fly decimation while preserving some directivity information. A final challenge of note is near-field coherent noise, for example roads or train lines [Dou et al., 2017, Lindsey et al., 2020b]. The back-migration method we present would be sensitive to coherent vehicle noise that would likely prevent simultaneous earthquake detection. A key benefit of fibreoptic sensing is measuring the seismic wavefield in urban environments, so going forward this challenge would have to be addressed for urban earthquake detection.

5.4 Future directions

The aforementioned challenges inspire directions for future work. Recording and processing large data volumes (TBs) is non-trivial and limits real-time earthquake detection using back-migration style algorithms. A possible avenue for reducing data volumes could be applying compressive-sensing based approaches [Muir and Zhan, 2021] to effectively reduce the number of fibre channels used while retaining sufficient information to detect seismicity. In a similar vain, using non-uniform or cascading coalescence search grids, inspired by those used for earthquake location and tomography [Lomax and Curtis, 2001, Thrastarson et al., 2024], could optimise memory usage and compute expense while refining peak coalescence values and hence detection. Another avenue of future work is reducing or removing noise. Recent advances applying machine learning to minimise instrument noise [Lapins et al., 2023] could readily be applied to our detection workflow, improving detection performance. A remaining endeavour is to perform masking of coherent noise sources. For example, certain regions of the coalescence search grid may correspond to roads that act as temporally-varying noise sources. One could envisage adapting our detection method to remove parts of the wavefield corresponding to a coalescence of energy from these locations, in a similar approach to that taken to mitigate fibreoptic sensitivity in this work. Simultaneously arriving lower SNR earthquakes may then be detectable even in the presence of higher local coherent noise sources.

6 CONCLUSIONS

Here, we describe adaptations made to a back-migration earthquake detection method required to process fibreoptic (DAS) receiver measurements. We show the inherent strengths of back-migration detection methods for harnessing the dense spatial sampling of the seismic wavefield that fibreoptic sensing provides. Such methods can be deployed for processing fibreoptic cables of arbitrary geometries. They also enable the combination of fibreoptic and conventional receivers to maximise the spatial extent and information used for detection. We also attempt to provide an overview of the current status of earthquake detection using fibreoptic sensing more generally, especially regarding identifying challenges provided by fibreoptic strain measurements and possible ways to overcome them. Finally, although the detection method presented here appears robust for earthquake detection in diverse geological settings, we briefly identify key remaining challenges and future directions that these challenges inspire.

ACKNOWLEDGMENTS

For the Gornergletscher dataset, the Sintella interrogator used was kindly borrowed from M. Kendall at the University of Oxford. We also want to thank T. Kettlety for helping set up the interrogator. F. Walter, E. Wolf, R. Cross and E. Julen provided support in the field, without which the experiment would not have been possible. The fieldwork was funded by a Leverhulme Early Career Fellowship ECF-2022-499) and Oxford University's John Fell Fund (0013666). A philanthropist kindly provided logistical support through use of a vehicle for the Gornergletscher fieldwork. For the Iceland DAS experiment, we thank HS Orka, operator of the Svartsengi Geothermal Power Station, for access to the fibreoptic cable. O.Fontaine is supported by FNRS (Fonds de la Recherche Scientifique, contract number: FC 49429). For the Utah FORGE experiment, we thank the project partners for making the data openly accessible.

DATA AVAILABILITY

Earthquake catalogues for each dataset are provided, along with a full working example of how to run the modified QuakeMigrate package, via an archived online repository [Hudson, 2024a]. The exact DAS modified version of the QuakeMigrate software is also archived online [Hudson, 2024b], which will be merged with the main QuakeMigrate repository in due course.. Data for the example earthquakes from the Gornergletscher glacier and the Iceland volcanic dataset are also provided in the same repository. Also provided in this repository are jupyter-notebook examples of running the modified version of QuakeMigrate. FORGE DAS data are available from US DOE Geothermal Data Repository (https://doi.org/10.15121/1603679) and seismometer data from the University of Utah (https://doi.org/10.7914/SN/UU), accessed from Incorporated Research Institutions for Seismology (https://ds.iris.edu/mda/UU/).

References

R. V. Allen. Automatic earthquake recognition and timing from single traces. *Bulletin of the Seismological Society of America*, 68(5):1521–1532, 1978.

A. F. Baird. Modelling the Response of Helically Wound DAS Cables to Microseismic Arrivals. In *First EAGE Workshop on Fibre Optic Sensing*, pages 1–5. European Association of Geoscientists Engineers, 2020. doi: 10.3997/2214-4609.202030019. URL `https://www.earthdoc.org/content/papers/10.3997/2214-4609.202030019`.

Y. Capdeville and A. Sladen. DAS sensitivity to heterogeneity scales much smaller than the minimum wavelength. *Seismica*, 3(1), jan 2024. ISSN 2816-9387. doi: 10.26443/seismica.v3i1.1007. URL `https://seismica.library.mcgill.ca/article/view/1007`.

N. L. Celli, C. J. Bean, and G. S. O'Brien. Full-waveform simulation of DAS records, response and cable-ground coupling. *Geophysical Journal International*, 236(1):659–674, jan 2024. ISSN 1365246X. doi: 10.1093/gji/ggad449.

S. Dou, N. Lindsey, A. M. Wagner, T. M. Daley, B. Freifeld, M. Robertson, J. Peterson, C. Ulrich, E. R. Martin, and J. B. Ajo-Franklin. Distributed Acoustic Sensing for Seismic Monitoring of the Near Surface: A Traffic-Noise Interferometry Case Study. *Scientific Reports*, 7(1):1–12,

2017. ISSN 20452322. doi: 10.1038/s41598-017-11986-4. URL http://dx.doi.org/10.1038/s41598-017-11986-4.

J. Drew, R. S. White, F. Tilmann, and J. Tarasewicz. Coalescence microseismic mapping. *Geophysical Journal International*, 195(3):1773–1785, 2013. ISSN 0956540X. doi: 10.1093/gji/ggt331.

A. Dzubay, M. Mesimeri, K. M. Whidden, D. Wells, and K. Pankow. Developing a comprehensive seismic catalog using a matched-filter detector during a 2019 stimulation at Utah FORGE. *47th Workshop on Geothermal Reservoir Engineering*, pages 1–9, 2022.

M. Guidarelli, P. Klin, and E. Priolo. Migration-based near real-time detection and location of microearthquakes with parallel computing. *Geophysical Journal International*, 221(3):1941–1958, 2020. ISSN 1365246X. doi: 10.1093/gji/ggaa111.

A. H. Hartog, L. B. Liokumovich, N. A. Ushakov, O. I. Kotov, T. Dean, T. Cuny, A. Constantinou, and F. V. Englich. The use of multi-frequency acquisition to significantly improve the quality of fibre-optic-distributed vibration sensing. *Geophysical Prospecting*, 66:192–202, 2018. ISSN 13652478. doi: 10.1111/1365-2478.12612.

A. Helmstetter, L. Moreau, B. Nicolas, P. Comon, and M. Gay. Intermediate-depth icequakes and harmonic tremor in an Alpine glacier (Glacier d'Argentière, France): Evidence for hydraulic fracturing. *Journal of Geophysical Research: Earth Surface*, 120(3):402–416, 2015. ISSN 21699011. doi: 10.1002/2014JF003289.

P. D. Hernandez, J. A. Ramirez, and M. A. Soto. Deep-Learning-Based Earthquake Detection for Fiber-Optic Distributed Acoustic Sensing. *Journal of Lightwave Technology*, 40(8):2639–2650, 2022. ISSN 15582213. doi: 10.1109/JLT.2021.3138724.

T. S. Hudson. Supplementary data for the article: ”Towards an widely applicable earthquake detection algorithm for fibreoptic and hybrid fibreoptic-seismometer networks”. *Zenodo*, 2024a. doi: 10.5281/zenodo.13355664.

T. S. Hudson. QuakeMigrate with DAS integration. *Zenodo*, 2024b. doi: 10.5281/zenodo.13355775.

T. S. Hudson, J. Smith, A. M. Brisbourne, and R. S. White. Automated detection of basal icequakes and discrimination from surface crevassing. *Annals of Glaciology*, 60(79):167–181, sep 2019. ISSN 0260-3055. doi: 10.1017/aog.2019.18. URL https://www.cambridge.org/core/product/identifier/S0260305519000181/type/journal_article.

T. S. Hudson, A. M. Brisbourne, R. S. White, J. M. Kendall, R. Arthern, and A. M. Smith. Breaking the Ice: Identifying Hydraulically Forced Crevassing. *Geophysical Research Letters*, 47(21), nov 2020. ISSN 0094-8276. doi: 10.1029/2020GL090597. URL https://onlinelibrary.wiley.com/doi/10.1029/2020GL090597.

T. S. Hudson, A. F. Baird, J. M. Kendall, S. K. Kufner, A. M. Brisbourne, A. M. Smith, A. Butcher, A. Chalari, and A. Clarke. Distributed Acoustic Sensing (DAS) for Natural Microseismicity Studies: A Case Study From Antarctica. *Journal of Geophysical Research: Solid Earth*, 126(7):1–19, 2021. ISSN 2169-9313. doi: 10.1029/2020jb021493.

T. S. Hudson, A. M. Brisbourne, S.-k. Kufner, J.-m. Kendall, and M. Smith. Array processing in cryoseismology. *The Cryosphere*, 2023. doi: 10.5194/egusphere-2023-657.

F. Huot, A. Lellouch, P. Given, B. Luo, R. G. Clapp, T. Nemeth, K. T. Nihei, and B. L. Biondi. Detection and Characterization of Microseismic Events from Fiber-Optic das Data Using Deep Learning. *Seismological Research Letters*, 93(5):2543–2553, 2022. ISSN 19382057. doi: 10.1785/0220220037.

F. Huot, R. G. Clapp, and B. L. Biondi. Detecting local earthquakes via fiber-optic cables in telecommunication conduits under Stanford University campus using deep learning. *Computers and Geosciences*, 190(May), 2024. ISSN 00983004. doi: 10.1016/j.cageo.2024.105625.

J. K. H. Igel, D. C. Bowden, and A. Fichtner. SANS: Publicly Available Daily Multi-Scale Seismic Ambient Noise Source Maps. *Journal of Geophysical Research: Solid Earth*, 128(1):1–22, jan 2023. ISSN 2169-9313. doi: 10.1029/2022JB025114. URL https://onlinelibrary.wiley.com/doi/10.1029/2022JB025114.

S. Lapins, A. Butcher, J.-M. Kendall, T. S. Hudson, A. L. Stork, M. J. Werner, J. Gunning, and A. M. Brisbourne. DAS-N2N: machine learning distributed acoustic sensing (DAS) signal denoising without clean data. *Geophysical Journal International*, 236(2):1026–1041, dec 2023. ISSN 0956-540X. doi: 10.1093/gji/ggad460. URL https://academic.oup.com/gji/

article/236/2/1026/7453669.

R. B. Latto, R. J. Turner, A. M. Reading, and J. P. Winberry. Towards the systematic reconnaissance of seismic signals from glaciers and ice sheets - Part 1: Event detection for cryoseismology. *Cryosphere*, 18(4):2061–2079, 2024. ISSN 19940424. doi: 10.5194/tc-18-2061-2024.

A. Lellouch, N. J. Lindsey, W. L. Ellsworth, and B. L. Biondi. Comparison between distributed acoustic sensing and geophones: Downhole microseismic monitoring of the FORGE geothermal experiment. *Seismological Research Letters*, 91(6):3256–3268, 2020. ISSN 19382057. doi: 10.1785/0220200149.

N. J. Lindsey and E. R. Martin. Fiber-Optic Seismology. *Annual Review of Earth and Planetary Sciences*, pages 309–336, 2021.

N. J. Lindsey, H. Rademacher, and J. B. Ajo-Franklin. On the Broadband Instrument Response of Fiber-Optic DAS Arrays. *Journal of Geophysical Research: Solid Earth*, 125(2):1–16, 2020a. ISSN 21699356. doi: 10.1029/2019JB018145.

N. J. Lindsey, S. Yuan, A. Lellouch, L. Gualtieri, T. Lecocq, and B. Biondi. City-Scale Dark Fiber DAS Measurements of Infrastructure Use During the COVID-19 Pandemic. *Geophysical Research Letters*, 47(16):1–8, 2020b. ISSN 19448007. doi: 10.1029/2020GL089931.

A. Lomax and A. Curtis. Fast, probabilistic earthquake location in 3D models using oct-tree importance sampling. In *Geophys. Res. Abstr*, volume 3, 2001.

E. R. Martin. Passive imaging and characterization of the subsurface with DAS. *PhD thesis*, 2018.

S. M. Mousavi, W. L. Ellsworth, W. Zhu, L. Y. Chuang, and G. C. Beroza. Earthquake transformer—an attentive deep-learning model for simultaneous earthquake detection and phase picking. *Nature Communications*, 11(1):3952, dec 2020. ISSN 2041-1723. doi: 10.1038/s41467-020-17591-w. URL http://dx.doi.org/10.1038/s41467-020-17591-whttp://www.nature.com/articles/s41467-020-17591-w.

J. B. Muir and Z. Zhan. Seismic wavefield reconstruction using a pre-conditioned wavelet-curvelet compressive sensing approach. *Geophysical Journal International*, 227(1):303–315, 2021. ISSN 1365246X. doi: 10.1093/gji/ggab222.

J. B. Muir and Z. Zhan. Wavefield-based evaluation of DAS instrument response and array design. *Geophysical Journal International*, 229(1):21–34, 2022. ISSN 1365246X. doi: 10.1093/gji/ggab439.

S. O'Neel, H. P. Marshall, D. E. McNamara, and W. T. Pfeffer. Seismic detection and analysis of icequakes at Columbia Glacier, Alaska. *Journal of Geophysical Research: Earth Surface*, 112 (3):1–14, 2007. ISSN 21699011. doi: 10.1029/2006JF000595.

P. Paitz, P. Edme, D. Gräff, F. Walter, J. Doetsch, A. Chalari, C. Schmelzbach, and A. Fichtner. Empirical investigations of the instrument response for distributed acoustic sensing (Das) across 17 octaves. *Bulletin of the Seismological Society of America*, 111(1):1–10, 2021. ISSN 19433573. doi: 10.1785/0120200185.

J. Porras, D. Pecci, G. M. Bocchini, S. Gaviano, M. De Solda, K. Tuinstra, F. Lanza, A. Tognarelli, E. Stucchi, and F. Grigoli. A semblance-based microseismic event detector for DAS data. *Geophysical Journal International*, 236(3):1716–1727, jan 2024. ISSN 0956-540X. doi: 10.1093/gji/ggae016.

C. Porter. ArcticDEM, Version 4.1. *Harvard Dataverse*, 2023. doi: 10.7910/DVN/3VDC4W,.

Z. E. Ross, Y. Yue, M. A. Meier, E. Hauksson, and T. H. Heaton. PhaseLink: A Deep Learning Approach to Seismic Phase Association. *Journal of Geophysical Research: Solid Earth*, 124 (1):856–869, 2019a. ISSN 21699356. doi: 10.1029/2018JB016674.

Z. E. Ross, Y. Yue, M. A. Meier, E. Hauksson, and T. H. Heaton. PhaseLink: A Deep Learning Approach to Seismic Phase Association. *Journal of Geophysical Research: Solid Earth*, 124 (1):856–869, 2019b. ISSN 21699356. doi: 10.1029/2018JB016674.

N. D. Selby. Improved Teleseismic Signal Detection at Small-Aperture Arrays. *Bulletin of the Seismological Society of America*, 101(4):1563–1575, aug 2011. ISSN 0037-1106. doi: 10.1785/0120100253. URL https://pubs.geoscienceworld.org/bssa/article/101/4/1563-1575/349509.

L. Seydoux, N. M. Shapiro, J. De Rosny, F. Brenguier, and M. Landès. Detecting seismic activity with a covariance matrix analysis of data recorded on seismic arrays. *Geophysical Journal International*, 204(3):1430–1442, 2016. ISSN 1365246X. doi: 10.1093/gji/ggv531.

F. Sigmundsson, M. Parks, H. Geirsson, A. Hooper, V. Drouin, K. S. Vogfjörd, B. G. Ófeigsson, S. H. M. Greiner, Y. Yang, C. Lanzi, G. P. De Pascale, K. Jónsdóttir, S. Hreinsdóttir, V. Tolpekin, H. M. Fririksdóttir, P. Einarsson, and S. Barsotti. Fracturing and tectonic stress drive ultra-rapid magma flow into dikes. *Science*, 383(6688):1228–1235, mar 2024. ISSN 0036-8075. doi: 10.1126/science.adn2838. URL https://www.science.org/doi/10.1126/science.adn2838.

J. D. Smith, R. S. White, J.-P. Avouac, and S. Bourne. Probabilistic earthquake locations of induced seismicity in the Groningen region, the Netherlands. *Geophysical Journal International*, 222(1):507–516, 2020. ISSN 0956-540X. doi: 10.1093/gji/ggaa179.

A. L. Stork, A. F. Baird, S. A. Horne, G. Naldrett, S. Lapins, J.-M. Kendall, J. Wookey, J. P. Verdon, A. Clarke, and A. Williams. Application of Machine Learning To Microseismic Event Detection in Distributed Acoustic Sensing (Das) Data. *Geophysics*, pages 1–53, 2020. ISSN 0016-8033. doi: 10.1190/geo2019-0774.1.

D. Strutz and A. Curtis. Variational Bayesian experimental design for geophysical applications: seismic source location, amplitude versus offset inversion, and estimating CO2 saturations in a subsurface reservoir. *Geophysical Journal International*, 236(3):1309–1331, 2024. ISSN 1365246X. doi: 10.1093/gji/ggad492.

S. Thrastarson, D. P. van Herwaarden, S. Noe, C. J. Schiller, and A. Fichtner. REVEAL: A Global Full-Waveform Inversion Model. *Bulletin of the Seismological Society of America*, 114 (3):1392–1406, 2024. ISSN 19433573. doi: 10.1785/0120230273.

T. Toledo, P. Jousset, H. Maurer, and C. Krawczyk. Optimized experimental network design for earthquake location problems: Applications to geothermal and volcanic field seismic networks. *Journal of Volcanology and Geothermal Research*, 391:106433, 2020. ISSN 03770273. doi: 10.1016/j.jvolgeores.2018.08.011. URL https://doi.org/10.1016/j.jvolgeores.2018.08.011.

F. Wagner, A. Tryggvason, R. Roberts, B. Lund, and Gudmundsson. Automatic seismic event detection using migration and stacking: A performance and parameter study in Hengill, southwest Iceland. *Geophysical Journal International*, 209(3):1866–1877, 2017. ISSN 1365246X.

doi: 10.1093/gji/ggx127.

F. Walter, J. F. Clinton, N. Deichmann, D. S. Dreger, S. E. Minson, and M. Funk. Moment tensor inversions of icequakes on Gornergletscher , Switzerland. *Bulletin of the Seismological Society of America*, 99(2):852–870, 2009. doi: 10.1785/0120080110.

F. Walter, D. Gräff, F. Lindner, P. Paitz, M. Köpfli, M. Chmiel, and A. Fichtner. Distributed Acoustic Sensing of Microseismic Sources and Wave Propagation in Glaciated Terrain. *Nature Communications*, 53(9):1689–1699, 2020. ISSN 1098-6596. doi: 10.1017/CBO9781107415324.004.

T. Winder, C. Bacon, J. D. Smith, T. S. Hudson, J. Drew, and R. S. White. QuakeMigrate v1.0.0 (v1.0.0). *Zenodo*, 2021. doi: 10.5281/zenodo.4442748.

M. Withers, R. Aster, C. Young, J. Beiriger, M. Harris, S. Moore, and J. Trujillo. A comparison of select trigger algorithms for automated global seismic phase and event detection. *Bulletin of the Seismological Society of America*, 88(1):95–106, 1998. ISSN 00371106.

W. Zhu and G. C. Beroza. PhaseNet: A deep-neural-network-based seismic arrival-time picking method. *Geophysical Journal International*, 216(1):261–273, 2019. ISSN 1365246X. doi: 10.1093/gji/ggy423.

W. Zhu, E. Biondi, J. Li, J. Yin, Z. E. Ross, and Z. Zhan. Seismic arrival-time picking on distributed acoustic sensing data using semi-supervised learning. *Nature Communications*, 14 (1):1–11, 2023. ISSN 20411723. doi: 10.1038/s41467-023-43355-3.

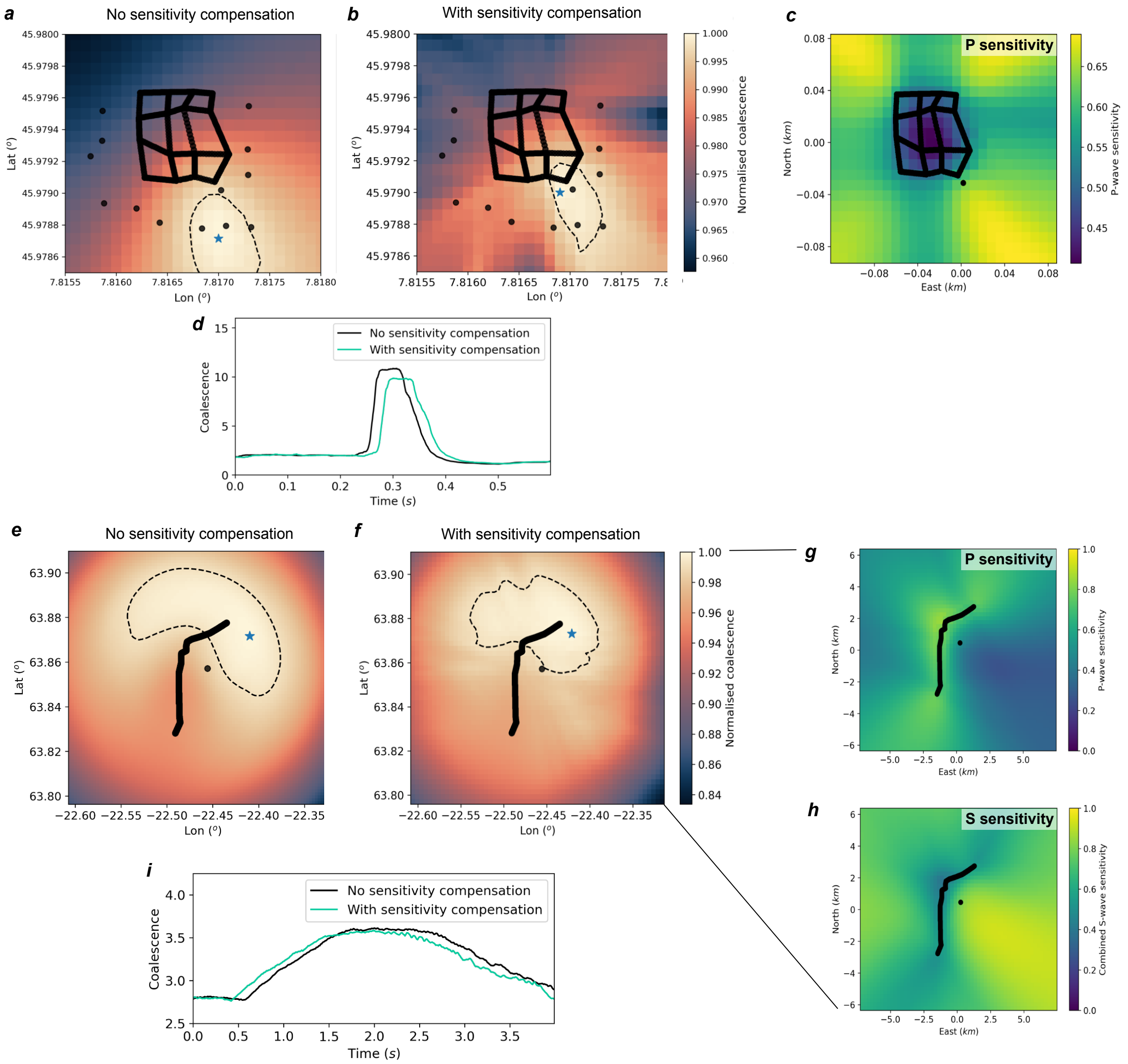

Figure 6. Effect of fibreoptic sensitivity on detection performance. a,b. Coalescence maps for a glacier icequake example, without and with sensitivity compensation, respectively. c. P-wave sensitivity map for the Gornergletscher network corresponding to the results of (b). d. Comparison of maximum single-pixel coalescence values through time with and without sensitivity compensation. e,f. Coalescence maps for a volcano-tectonic example, without and with sensitivity compensation, respectively. g,h. P- and S- wave sensitivity maps, respectively, for the Reykjanes Peninsula network corresponding to the results of (e). For each channel and seismic phase, regions with sensitivities < 0.1 are masked for individual receivers. i. Same as (d) but for the volcano-tectonic example.

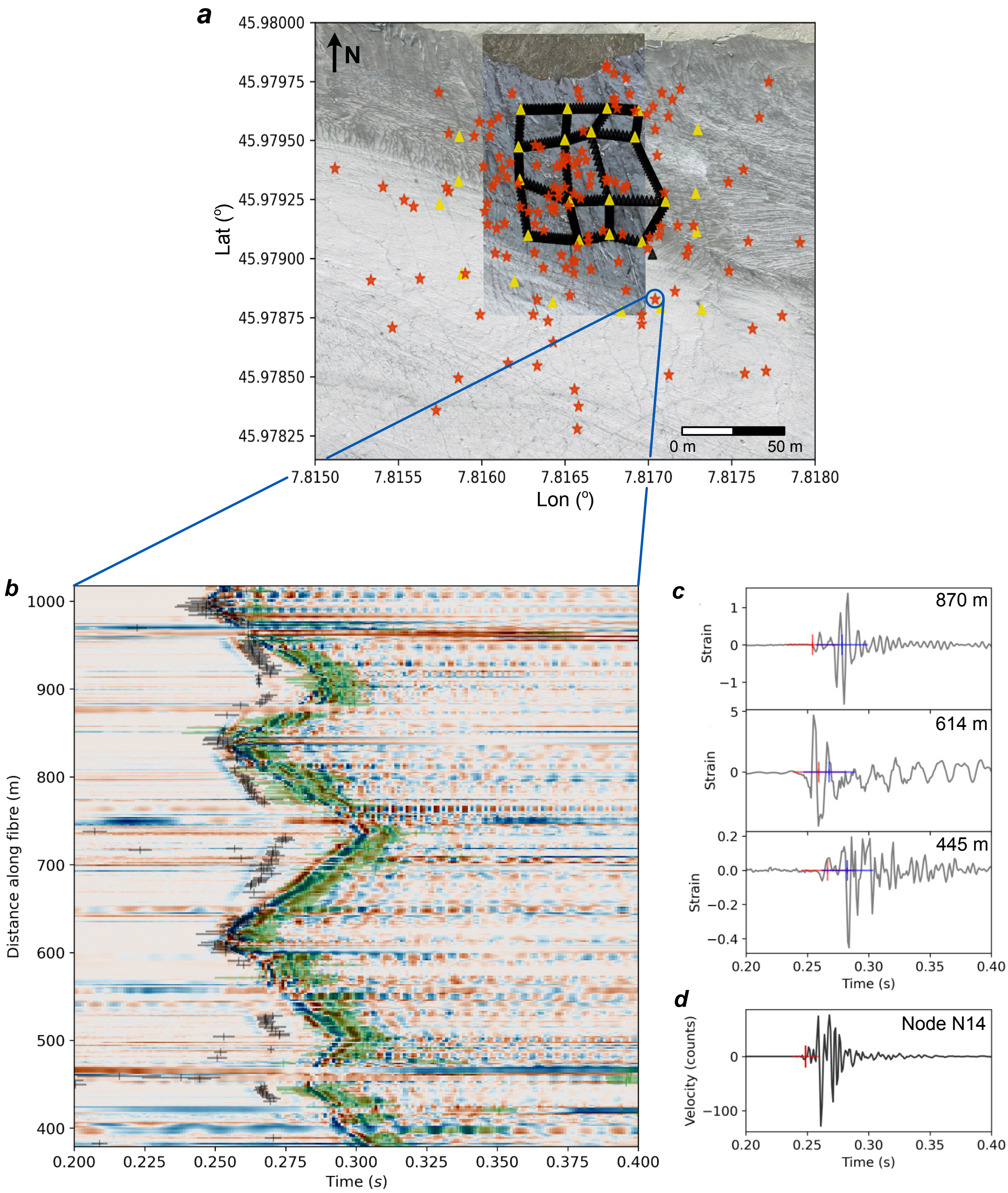

Figure 7. Glacier example from a crevasse field at Gornergletscher, Switzerland. a. Gornergletscher icequake catalogue (2023-10-22T04:00:00 to 2023-10-22T10:00:00). Red stars are icequakes, black triangles are DAS channels and gold triangles are seismic nodes. Background images are from an unmanned aerial vehicle during field deployment and from Swiss Topo (accessed: 10^{th} June 2024). b. Example icequake signal measured on the fibre. Colours are normalised strain. Black and green scatter points show P-wave and surface-wave arrival time picks, respectively, by QuakeMigrate. c. Phase arrival picks for P-waves (red) and surface-waves (blue) for three channels in more detail. d. Example of P-wave arrival detected on a seismic vertical single-component node for comparison.

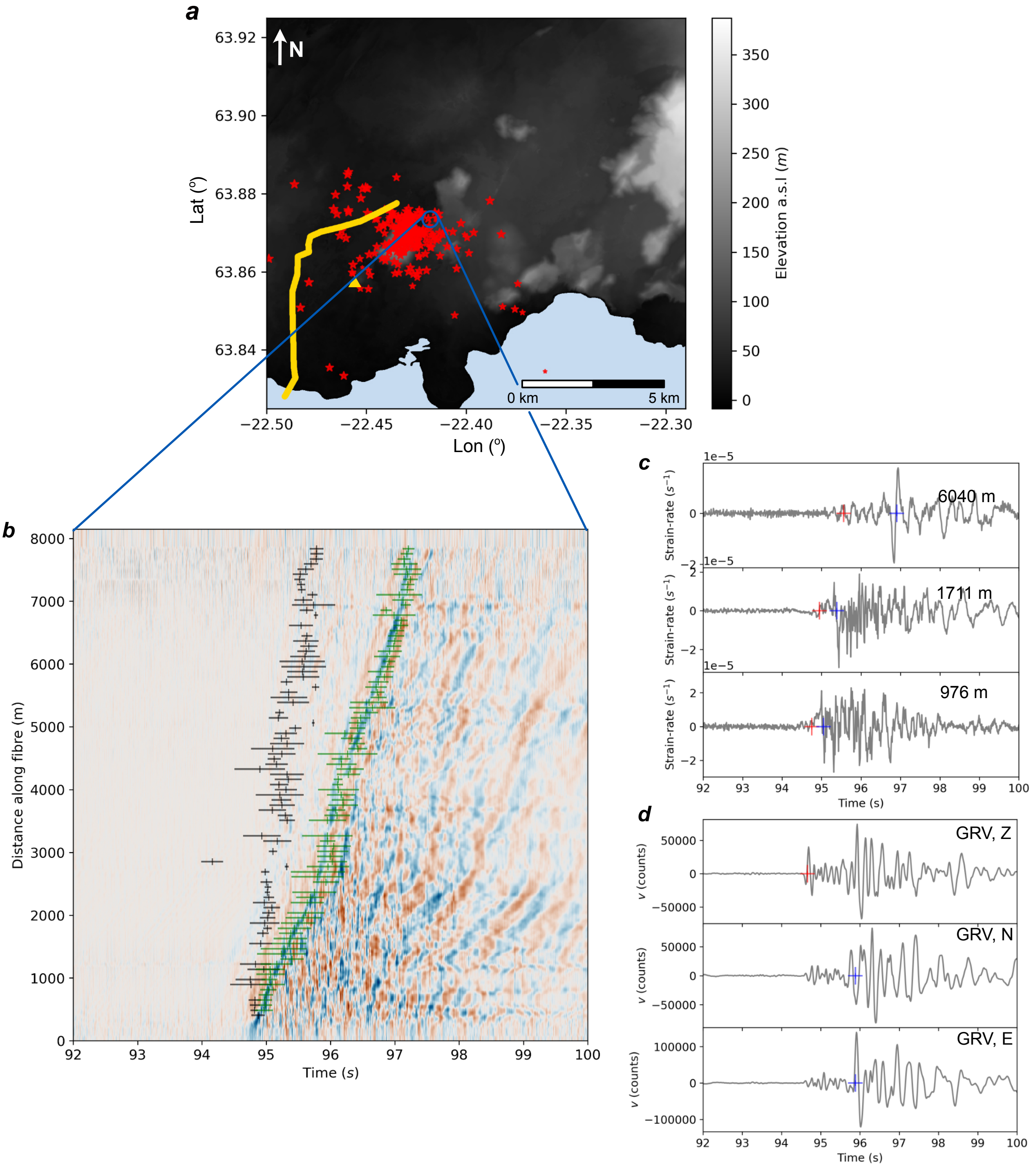

Figure 8. Volcanic eruption example from Sundhnúkagígar on the Reykjanes Peninsula, Iceland. a. Earthquake catalogue from one eruptive period (2023-12-18T00:00:00.0 to 2023-12-20T00:00:00.0). Fibre receivers are shown by gold line, seismometer receiver is shown by gold triangle, earthquakes detected and located in this study are red stars and matched Icelandic Met Office events are shown by blue stars. Digital elevation model is from the ArcticDEM [Porter, 2023]. b. Example earthquake signal measured on the fibre. Colours are normalised strain-rate. Black and green scatter points show P-wave and S-wave arrival time picks, respectively, by QuakeMigrate. c. Phase arrival picks for P-waves (red) and S-waves (blue) for three channels in more detail. d. Example of P-wave and S-wave arrivals detected on a conventional seismometer operated by IMO, for comparison.

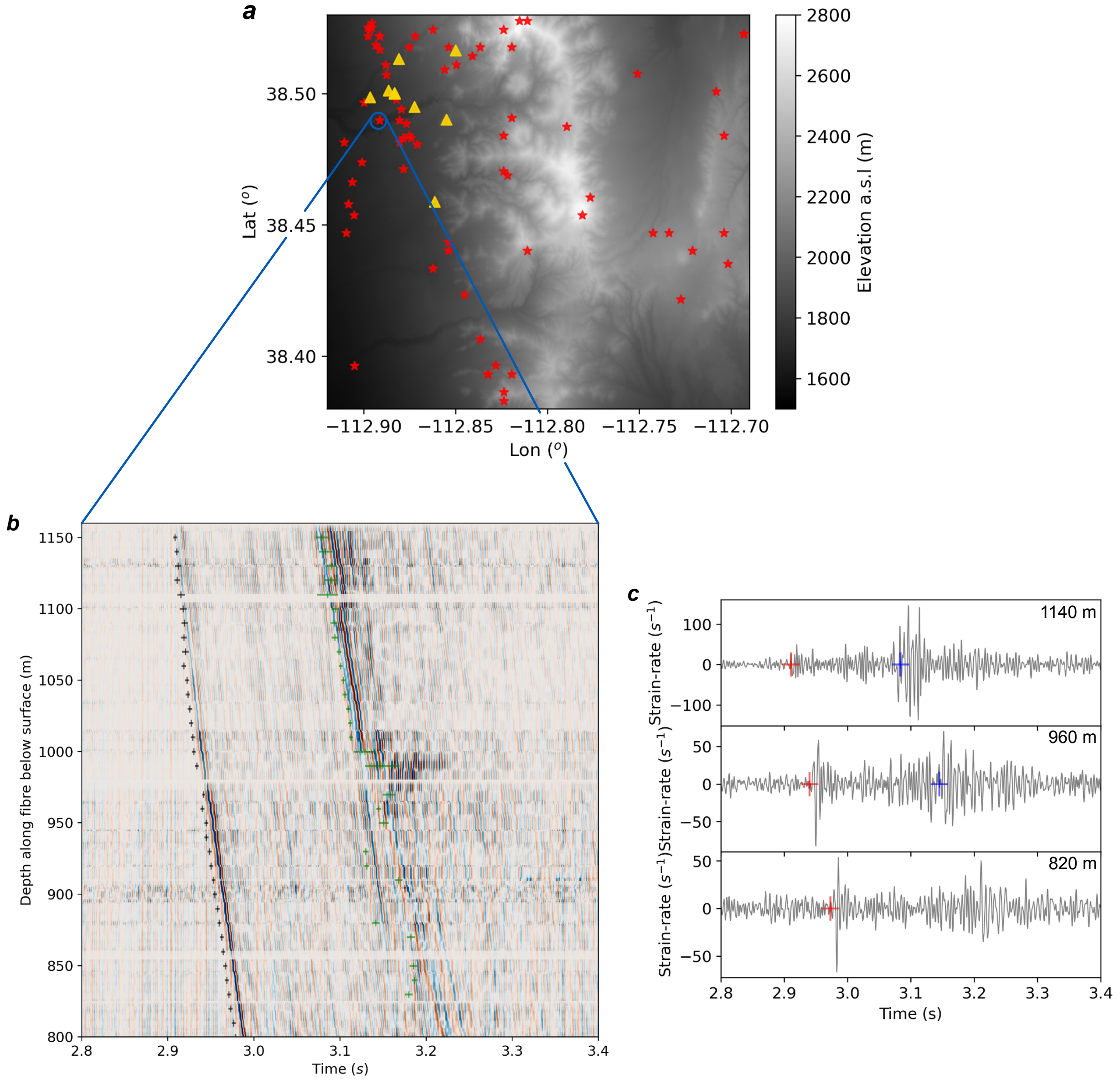

Figure 9. Geothermal borehole example from the Utah FORGE experiment, US. a. Earthquake catalogue from a one hour period during stimulation (17:00 to 18:00 on 27^{th} April 2019). Receivers are shown by gold triangles and earthquakes detected and located in this study are red stars. Digital elevation model is from the NASA Shuttle Radar Topography Mission (SRTM). b. Example earthquake signal measured on the fibre. Colours are normalised strain-rate. Black and green scatter points show P-wave and S-wave arrival time picks, respectively, by QuakeMigrate. c. Phase arrival picks for P-waves (red) and S-waves (blue) for three channels in more detail.